

Anomalous Nonreciprocal Electrical Transport on Chiral Magnetic Order

Ryuya Aoki,¹ Yusuke Kousaka,² and Yoshihiko Togawa¹¹Department of Physics and Electronics, Osaka Prefecture University, 1-1 Gakuencho, Sakai, Osaka 599-8531, Japan²Research Institute for Interdisciplinary Science, Okayama University, Okayama, Okayama 700-8530, Japan

(Received 5 September 2018; published 8 February 2019)

Nonreciprocal flow of conduction electrons is systematically investigated in a monoaxial chiral helimagnet CrNb₃S₆. We found that such directional dichroism of the electrical transport phenomena, called the electrical magnetochiral (EMC) effect, occurs in a wide range of magnetic fields and temperatures. The EMC signal turns out to be considerably enhanced below the magnetic ordering temperature, suggesting a strong influence of the chiral magnetic order on this anomalous EMC transport property. The EMC coefficients are separately evaluated in terms of crystalline and magnetic contributions in the magnetic phase diagram.

DOI: 10.1103/PhysRevLett.122.057206

Chiral structures play an important role in inducing a variety of striking physical responses. For instance, optical rotation and circular dichroism occur in chiral media being illuminated by polarized electromagnetic (EM) waves. Recently, in addition to a natural optical activity, directional dichroism, in which the absorption of incident EM waves differs when reversing a propagation direction of the EM waves in the presence of a magnetic field, has attracted considerable interest. Indeed, this remarkable phenomenon has been observed in a range of frequencies of the EM waves including visible light [1–3], x ray [4], and microwave [5,6]. Such directional dichroism or nonreciprocal response has also been discussed in transport phenomena of quasiparticles such as magnons [7,8] and phonons [9] in noncentrosymmetric crystals under the influence of a magnetic field.

Nonreciprocal transport of conduction electrons, frequently called the electrical magnetochiral (EMC) effect [10–16], is phenomenologically expressed by

$$R(\mathbf{H}, \mathbf{I}) = R_0(1 + \gamma\mu_0\mathbf{H} \cdot \mathbf{I}). \quad (1)$$

The second term on the right-hand side corresponds to the EMC resistance R_{EMC} and indicates an electrical resistance dependent on the directions of the external magnetic field \mathbf{H} and electric current \mathbf{I} . Here, γ is the R_{EMC} coefficient and its sign is associated with structural chirality. The magnitude of R_{EMC} alters in accordance with four combinations of \mathbf{H} and \mathbf{I} directions when both orient toward the helical axis, as schematically drawn in Fig. 1(a).

Chiral helimagnetic materials can host topological spin structures such as chiral helimagnetic order [17,18], chiral conical structure, chiral soliton lattice (CSL) [19,20], and chiral magnetic skyrmions [21–23], as partially illustrated in Fig. 1(b). Importantly, nontrivial transport phenomena are induced through the coupling of itinerant electrons with

the chiral magnetic order [24,25], as exemplified by discrete magnetoresistance (MR) [26] or topological Hall effect [27]. In this respect, it is quite interesting to learn how the chiral magnetic order influences nonreciprocal transport phenomena.

The EMC effect was recently investigated in a cubic chiral helimagnet MnSi which contains multiple helical axes and may allow the formation of domain structures of the chiral magnetic order [14]. It was reported that the EMC

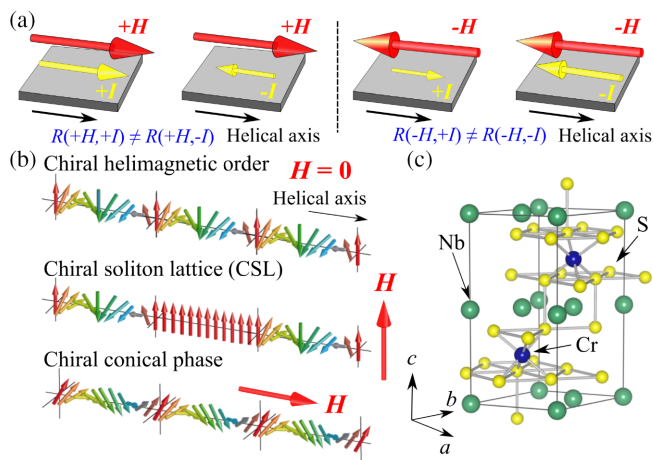


FIG. 1. Schematics of the EMC effect (a), chiral magnetic order (b), and a crystal structure of CrNb₃S₆ (c). Nonreciprocal flow of conduction electrons occurs along the helical axis in the presence of H . The EMC resistance amplitude varies depending on the directions of H and I , respectively indicated by red and yellow bold arrows, with respect to the helical axis (black thin arrow). The change in the electric current amplitude occurs when measuring the EMC resistance with the constant voltage applied, as schematically illustrated by the size of yellow arrows in (a). Alternatively, the EMC voltage changes are detected with the current amplitude fixed in this study.

signal is enhanced at large fields above the critical temperature T_c . This enhancement is ascribed to chiral spin fluctuations induced in a crossover region between the paramagnetic (PM) phase and the forced ferromagnetic (FM) phase. However, the EMC intensity appears to be significantly suppressed at low magnetic fields and temperatures where the chiral conical phase and chiral magnetic skyrmions are predominantly formed. Thus, the contribution of the chiral magnetic order to the EMC effect was not clear in the previous experiment.

In this Letter, the nonreciprocal EMC transport properties are investigated in a prototype monoaxial chiral helimagnet CrNb_3S_6 . We revealed that drastic changes of the EMC response are driven upon the formation of the chiral magnetic order. The EMC signal is considerably enhanced in the chiral conical phase and the R_{EMC} takes its maximum absolute value just below T_c . The crystalline and magnetic counterparts of the EMC response are separately detected in a wide range of magnetic fields and temperatures. The magnetic term turns out to be about 3 orders of magnitude larger than the crystalline term, thereby causing the anomalous EMC response on the chiral magnetic order.

The monoaxial chiral helimagnet CrNb_3S_6 has a crystal structure consisting of hexagonal planes of NbS_2 and intercalated Cr atoms, as illustrated in Fig. 1(c). It belongs to the space group $P6_322$. The principal (c) axis of the crystal is coincident with the single helimagnetic axis observed in this compound.

The magnetic phase diagram of CrNb_3S_6 consists of the CSL and chiral conical phases. Advantageously, only the chiral conical phase emerges without accompanying any domain structure and hysteresis effect in magnetic fields applied in the direction parallel to the c axis [28]. In addition, the CSL, which appears in magnetic fields applied perpendicular to the c axis, makes no contribution to the EMC signal because it has magnetic moments rotating only within the ab plane and induces no effective field along the c axis. Thus, the CSL will work as an ideal reference state to the chiral conical phase when studying the EMC effect.

CrNb_3S_6 bulk crystals were grown using a chemical-vapor transport method, as described elsewhere [29]. A micrometer-sized platelet specimen was cut from the bulk single crystal used in Ref. [28] by focused ion beam methods. The sample was picked out from a particular region, around which many micrometer-sized lamella crystals were prepared for Lorentz microscopy observations [20] and the magnetic chirality of those samples was identified as left-handed. Thus, the present sample presumably possesses the left-handed magnetic chirality. These microscopic observations also indicate that the sample has a homochiral crystalline structure since there is a close correlation between the structural chirality and magnetic chirality in chiral magnetic crystals [30]. The sample size is $13.5 \times 8.5 \times 0.5 \mu\text{m}^3$. Gold electrodes for four-terminal resistance measurements were fabricated in

the sample by using electron beam lithography and liftoff techniques. The critical temperature is determined to be 121 K by the electrical resistance measurements, which also provided field and temperature information regarding the phase boundaries among the PM, forced FM, and chiral conical phases [31].

When an ac current $I = I_0 \sin \omega t$ is applied to the sample, a nonlinear EMC voltage is induced, as expressed by

$$V_{\text{EMC}}(t) = IR_{\text{EMC}} = \frac{\gamma}{2} \mu_0 R_0 I_0^2 H \left[1 - \sin \left(2\omega t + \frac{\pi}{2} \right) \right]. \quad (2)$$

The second harmonic resistance $R^{2\omega}$ was measured in order to detect the R_{EMC} using a lock-in technique with an ac current whose frequency was 13 Hz. The maximum amplitude of the current was set to 4.5 mA, corresponding to a current density of $1.1 \times 10^9 \text{ A/m}^2$. The Joule heating effect was negligibly small at this value.

The measurements were performed as a function of the applied magnetic field at various temperatures in a configuration where H and I were parallel to the c axis, as shown in Fig. 1(a). The angular dependence of $R^{2\omega}$ was also examined by changing the H direction within the sample plane with regards to the c axis. During the measurements, it was confirmed that the $R^{2\omega}$ exhibited $\pi/2$ phase shift against the first harmonic input. The measured $R^{2\omega}$ showed a field-dependent behavior and contained both even and odd components with regards to zero magnetic field. The former was the background derived from asymmetry of the electrode geometry, while the latter was ascribed to the R_{EMC} signal as presented in the following. More precisely, the R_{EMC} signal was obtained by calculating $[R^{2\omega}(H, I) - R^{2\omega}(-H, I)]/2$.

Figure 2(a) shows the calculated data as a function of H above T_c . A linear dependence of the signal on the field strength is clearly observed at 200 K, which is consistent with the behavior expected for the R_{EMC} of chiral non-magnetic materials [10,12] and indicates the high quality of the sample. Namely, since a racemic crystal is not able to exhibit such data, a homochiral crystalline single domain is obtained in the sample. With decreasing temperature T to 170 and 150 K, the R_{EMC} signal starts to grow. Moreover, it becomes nonlinear and even oscillated as T approaches T_c .

The R_{EMC} behavior changes drastically below T_c . Figures 2(b)–2(d) show several notable features: a sign reversal of the R_{EMC} when below T_c , sharp peaks in the vicinity of T_c (at 90–120 K), a reduction of the intensity at lower T (30–70 K), and its recovery at the lowest T regime (below 20 K).

Figure 2(e) shows a temperature dependent R_{EMC} at various magnetic fields. It is clear that the R_{EMC} signal takes negative and positive peaks above and below T_c , respectively. In addition, the signal becomes stronger below 20 K at larger fields, as seen in Fig. 2(d).

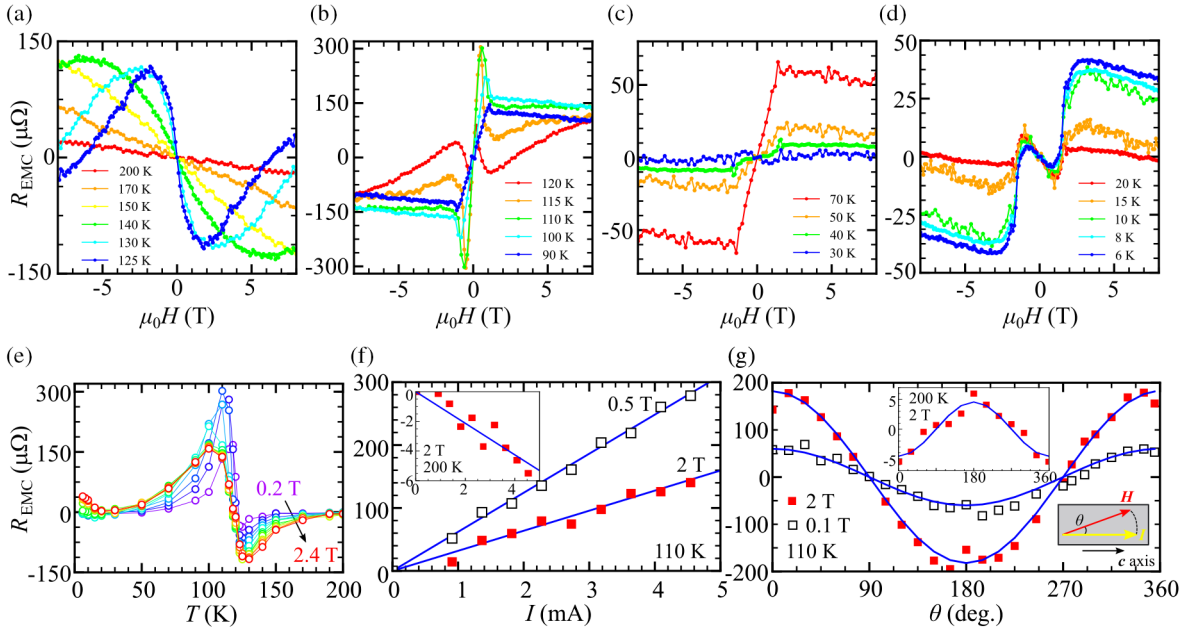


FIG. 2. A dataset of the R_{EMC} measurements performed in a CrNb_3S_6 crystal. (a)–(d) H dependence of R_{EMC} at 4.5 mA in a wider range of temperatures. (e) T dependent R_{EMC} at 4.5 mA from 0.2 to 2.4 T with an interval of 0.2 T. (f) R_{EMC} as a function of I at 0.5 T and 2 T at 110 K. The solid lines provide linear fitting curves. The inset shows the data at 200 K. (g) Angular dependence of R_{EMC} at 0.1 T and 2 T at 110 K with cosine fitting curves. The insets present the data at 200 K and a geometrical relationship of H , I , θ , and c axis of the platelet specimen.

The obtained R_{EMC} signal presents the behavior expected based on Eq. (1). The signal intensity increases in proportion to the current magnitude in the chiral conical and forced FM phases as well as in the PM phase, as seen in Fig. 2(f). An angular dependence of R_{EMC} in Fig. 2(g) clarified that the data are well fitted by cosine curves. These observations guarantee the validity of Eq. (1) irrespective of T . When H is applied perpendicular to I and the c axis, the R_{EMC} signal is almost absent, as expected for the behavior of the CSL phase. This result also indicates that the signal is not due to the voltage derived from the Nernst effect caused by Joule heating and justifies that the present data arise from the EMC effect.

Figure 3(a) presents the color contour map of the R_{EMC} intensity together with phase boundary lines. As seen in Fig. 2, the sign of R_{EMC} changes abruptly across the phase boundary between the PM and forced FM phases. The R_{EMC} signal is largely enhanced below T_c , taking the maximum value of about $300 \mu\Omega$ in the chiral conical phase. In the chiral conical phase, the amplitude of R_{EMC} reduces and its sign changes with decreasing T . A reduction in the amplitude is also seen in the forced FM phase as T decreases. However, the R_{EMC} remains positive and increases again below 20 K.

To see the R_{EMC} data in more detail, the normalized EMC coefficient $\hat{\gamma}$ is evaluated on all the magnetic phases, as shown in Fig. 3(b). Here, $\hat{\gamma}$ is given by $\hat{\gamma} = \gamma S = (S/\mu_0 R_0 I) \times \partial R_{EMC}/\partial H$, which follows Eq. (1) and is useful for analyzing the EMC effect of chiral nonmagnetic

materials. The term S corresponds to the cross-sectional area of the sample.

Negative $\hat{\gamma}$ values are found in the PM phase as well as in the forced FM phase and in the low T regime of the chiral conical phase of the present sample. In general, a magnetic contribution is largely suppressed in the PM phase with increasing T , and thus the R_{EMC} observed far above T_c should be induced mainly by the conventional EMC effect associated with chiral structures, as observed in chiral nonmagnetic materials [10,12]. The value of $\hat{\gamma}$ is approximately $-10^{-14} \text{ m}^2 \text{ T}^{-1} \text{ A}^{-1}$ at around 200 K in the PM phase (a region colored in light blue), although it increases by 1 order of magnitude with approaching T_c (highlighted in blue). Note that a typical value of the negative $\hat{\gamma}$ obtained below T_c is as large as $-10^{-14} \text{ m}^2 \text{ T}^{-1} \text{ A}^{-1}$, which is in the same magnitude as the value obtained at 200 K. This result suggests that the negative $\hat{\gamma}$ term is originated from the crystalline chirality. It underlies in all the regions irrespective of T and makes a contribution in reducing the R_{EMC} even in the chiral conical and forced FM phases.

Meanwhile, the positive $\hat{\gamma}$ term becomes prominent in three regions in which the chiral magnetic order including spin fluctuations emerges. The first region is the crossover regime between the PM and forced FM phases. The second is the chiral conical phase, which exhibits large positive $\hat{\gamma}$ except for at small H and low T . The maximum value of about $-10^{-12} \text{ m}^2 \text{ T}^{-1} \text{ A}^{-1}$ is obtained in the vicinity of T_c . The nonreciprocal EMC transport develops significantly in this regime. Finally, the positive $\hat{\gamma}$ is found around the phase

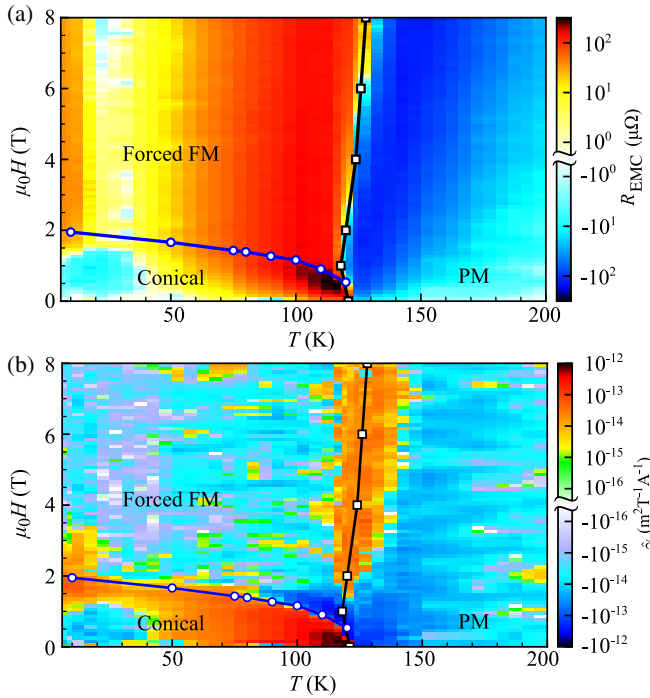


FIG. 3. Color contour maps of R_{EMC} (a) and EMC coefficient $\hat{\gamma}$ (b), drawn on the magnetic phase diagram of a CrNb_3S_6 crystal. Blue circles and black squares provide the phase boundaries determined by H and T dependent electrical resistance data, respectively [31].

boundary between the chiral conical phase and the forced FM one at the low T regime. Although the magnitude of $\hat{\gamma}$ varies depending on the regions, it is natural to consider that the positive $\hat{\gamma}$ term has the magnetic origin.

To distinguish crystalline and magnetic counterparts explicitly, the R_{EMC} data below T_c are analyzed using the following empirical equation:

$$R_{\text{EMC}} = R_{\text{EMC}}^{\text{cryst}} + R_{\text{EMC}}^{\text{mag}} = \mu_0 R_0 I (\gamma_{\text{cryst}} H + \gamma_{\text{mag}} M). \quad (3)$$

This equation includes the magnetic term, which varies in proportion to the magnetization M of the magnetic state, as frequently discussed in the anomalous Hall effect [33].

Figure 4(b) presents the EMC data below and above T_c , which are respectively fitted by using Eq. (3) and the conventional equation without the $R_{\text{EMC}}^{\text{mag}}$ term (for details, see Supplemental Material [31]). A contour map of the signal intensity deviated from the linear behavior, ΔR_{EMC} , is provided on the magnetic phase diagram in Fig. 4(c). Five regions are clearly identified. Regions II and V present the linear R_{EMC} behavior. On the other hand, the signal deviation ΔR_{EMC} becomes significant in regions I, III, and IV. Namely, nonlinear and field-dependent magnetic terms are required for inducing the R_{EMC} behavior in those regions.

The normalized $\hat{\gamma}_{\text{cryst}}$ and $\hat{\gamma}_{\text{mag}}$ as a function of temperature are presented in Fig. 4(d). In region IV, the R_{EMC}

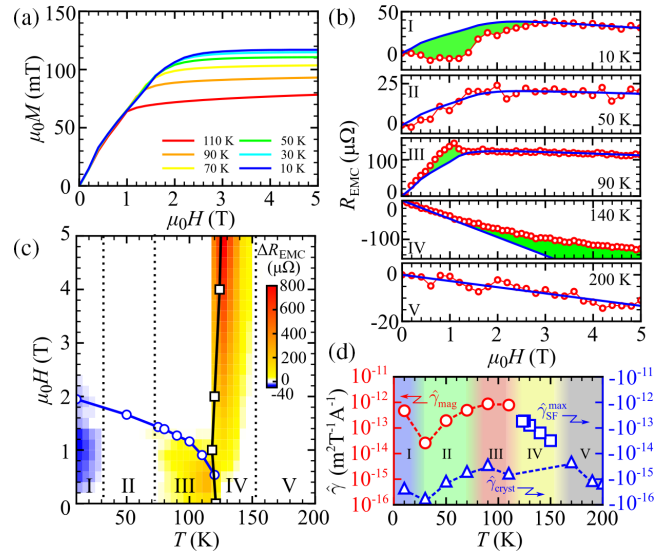


FIG. 4. (a) Magnetization curves of a CrNb_3S_6 crystal in H applied parallel to the c axis at various temperatures. (b) R_{EMC} data with the fitting curves. The areas highlighted in light green indicate the signal deviated from the linear behavior, which corresponds to the nonlinear contribution ΔR_{EMC} . (c) A color contour map of ΔR_{EMC} on the magnetic phase diagram. Five regions labeled by I–V are identified with the criteria of $\pm 10 \mu\Omega$. (d) Temperature dependence of the EMC coefficients. Note that $\hat{\gamma}_{\text{mag}}$ takes positive values while $\hat{\gamma}_{\text{cryst}}$ and $\hat{\gamma}_{\text{SF}}^{\text{max}}$ take negative values in this sample.

behavior is characterized by the maximum slope in the limit of zero magnetic field ($\hat{\gamma}_{\text{SF}}^{\text{max}}$). The absolute values for $\hat{\gamma}_{\text{mag}}$ turn out to be about 3 orders of magnitude larger than those for $\hat{\gamma}_{\text{cryst}}$, while the sign of them is opposite. The magnitude of $\hat{\gamma}_{\text{SF}}^{\text{max}}$ is also enhanced with regards to $\hat{\gamma}_{\text{cryst}}$ and its behavior is likely to interpolate between $\hat{\gamma}_{\text{mag}}$ in region III and $\hat{\gamma}_{\text{cryst}}$ in region V.

Possible origins of the EMC effect have been discussed in the literature [10]. One is a self-magnetic-field effect caused by a current-induced magnetic field on a chiral framework, which induces the R_{EMC} linearly dependent on H with the crystalline term $\hat{\gamma}_{\text{cryst}}$. The other is a nonlinear chiral scattering of conduction electrons due to chiral spin fluctuations, as discussed in MnSi [34–37]. Similar critical phenomena have been found in many chiral helimagnets such as FeGe [38–40], Cu_2OSeO_3 [41], and CrNb_3S_6 [42–44]. The response of this regime is supposed to be larger than the conventional EMC response, which is consistent with the experimental results that $\hat{\gamma}_{\text{SF}}^{\text{max}}$ is larger than $\hat{\gamma}_{\text{cryst}}$. These two mechanisms can explain characteristics of the R_{EMC} in the PM phase. However, they do not appear to work as the EMC mechanism which is compatible with the chiral magnetic order. In particular, the nonlinear R_{EMC} behavior, prominent in regions I and III, is beyond the expected behavior based on Eq. (3). Theoretical considerations on the microscopic origin of

the anomalous EMC response including thermal influences are eagerly required.

Quite recently, a band structure of CrNb_3S_6 calculated using density functional theory [45] revealed that the coupling of spin polarization and orbital angular momentum causes a peculiar shift of band dispersions in k space and results in a highly asymmetric Fermi surface when the magnetization is aligned parallel to the c axis at zero temperature. This may induce nonreciprocal EMC transport at the low T regime in the forced FM phase in CrNb_3S_6 . Such nonreciprocal EMC transport induced by the band splitting was also discussed in a polar semiconductor BiTeBr [13].

In conclusion, nonreciprocal electrical transport phenomena were intensively examined in a monoaxial chiral magnet CrNb_3S_6 . The EMC response changes drastically upon the formation of the chiral magnetic order. In addition to the conventional EMC signal due to structural chirality, an anomalous enhancement of the R_{EMC} was found in the chiral conical phase, where the value of $\hat{\gamma}_{\text{mag}}$ is 3 orders of magnitude larger than that of $\hat{\gamma}_{\text{cryst}}$. These observations will provide a new insight on the interplay between structural and magnetic chirality on the nonreciprocal transport phenomena. Thorough investigations of the anomalous EMC effect in a material class of monoaxial chiral helimagnetic systems such as CrNb_3S_6 and YbNi_3Al_9 [46] may lead to further understanding of a wide variety of chirality-related phenomena in chiral magnetic materials.

We thank T. Arima, J. Kishine, I. Proskurin, K. Inoue, J. Akimitsu, H. Shishido, and T. Shishidou for useful discussions and F. J. T. Goncalves for a critical reading of the manuscript. We acknowledge support from Grants-in-Aid for Scientific Research (No. 25220803, No. 17H02767, No. 17H02923) and JSPS Core-to-Core Program, A. Advanced Research Networks. This work was also supported by Chirality Research Center (Crescent) in Hiroshima University.

-
- [1] G. L. J. A. Rikken and E. Raupach, Observation of magneto-chiral dichroism, *Nature (London)* **390**, 493 (1997).
- [2] M. Saito, K. Ishikawa, K. Taniguchi, and T. Arima, Magnetic Control of Crystal Chirality and the Existence of a Large Magneto-Optical Dichroism Effect in CuB_2O_4 , *Phys. Rev. Lett.* **101**, 117402 (2008).
- [3] N. Nakagawa, N. Abe, S. Toyoda, S. Kimura, J. Zaccaro, I. Gautier-Luneau, D. Luneau, Y. Kousaka, A. Sera, M. Sera, K. Inoue, J. Akimitsu, Y. Tokunaga, and T. Arima, Magneto-chiral dichroism of CsCuCl_3 , *Phys. Rev. B* **96**, 121102 (2017).
- [4] J. Goulon, A. Rogalev, F. Wilhelm, C. Goulon-Ginet, P. Carra, D. Cabaret, and C. Brouder, X-Ray Magneto-chiral Dichroism: A New Spectroscopic Probe of Parity Non-conserving Magnetic Solids, *Phys. Rev. Lett.* **88**, 237401 (2002).
- [5] Y. Okamura, F. Kagawa, S. Seki, M. Kubota, M. Kawasaki, and Y. Tokura, Microwave Magneto-chiral Dichroism in the Chiral-Lattice Magnet Cu_2OSeO_3 , *Phys. Rev. Lett.* **114**, 197202 (2015).
- [6] Y. Nii, R. Sasaki, Y. Iguchi, and Y. Onose, Microwave magneto-chiral effect in the non-centrosymmetric magnet CuB_2O_4 , *J. Phys. Soc. Jpn.* **86**, 024707 (2017).
- [7] Y. Iguchi, S. Uemura, K. Ueno, and Y. Onose, Nonreciprocal magnon propagation in a noncentrosymmetric ferromagnet LiFe_5O_8 , *Phys. Rev. B* **92**, 184419 (2015).
- [8] S. Seki, Y. Okamura, K. Kondou, K. Shibata, M. Kubota, R. Takagi, F. Kagawa, M. Kawasaki, G. Tatara, Y. Otani, and Y. Tokura, Magneto-chiral nonreciprocity of volume spin wave propagation in chiral-lattice ferromagnets, *Phys. Rev. B* **93**, 235131 (2016).
- [9] A. A. Tereshchenko, A. S. Ovchinnikov, I. Proskurin, E. V. Sinitsyn, and J. Kishine, Theory of magnetoelastic resonance in a monoaxial chiral helimagnet, *Phys. Rev. B* **97**, 184303 (2018).
- [10] G. L. J. A. Rikken, J. Fölling, and P. Wyder, Electrical Magneto-chiral Anisotropy, *Phys. Rev. Lett.* **87**, 236602 (2001).
- [11] V. Krstić, S. Roth, M. Burghard, K. Kern, and G. L. J. A. Rikken, Magneto-chiral anisotropy in charge transport through single-walled carbon nanotubes, *J. Chem. Phys.* **117**, 11315 (2002).
- [12] F. Pop, P. Senzier, E. Canadell, G. L. J. A. Rikken, and N. Avarvari, Electrical magneto-chiral anisotropy in a bulk chiral molecular conductor, *Nat. Commun.* **5**, 3757 (2014).
- [13] T. Ideue, K. Hamamoto, S. Koshikawa, M. Ezawa, S. Shimizu, Y. Kaneko, Y. Tokura, N. Nagaosa, and Y. Iwasa, Bulk rectification effect in a polar semiconductor, *Nat. Phys.* **13**, 578 (2017).
- [14] T. Yokouchi, N. Kanazawa, A. Kikkawa, D. Morikawa, K. Shibata, T. Arima, Y. Taguchi, F. Kagawa, and Y. Tokura, Electrical magneto-chiral effect induced by chiral spin fluctuations, *Nat. Commun.* **8**, 866 (2017).
- [15] F. Qin, W. Shi, T. Ideue, M. Yoshida, A. Zak, R. Tenne, T. Kikitsu, D. Inoue, D. Hashizume, and Y. Iwasa, Superconductivity in a chiral nanotube, *Nat. Commun.* **8**, 14465 (2017).
- [16] R. Wakatsuki, Y. Saito, S. Hoshino, Y. M. Itahashi, T. Ideue, M. Ezawa, Y. Iwasa, and N. Nagaosa, Nonreciprocal charge transport in noncentrosymmetric superconductors, *Sci. Adv.* **3**, e1602390 (2017).
- [17] I. E. Dzyaloshinskii, A thermodynamic theory of weak ferromagnetism of antiferromagnetics, *J. Phys. Chem. Solids* **4**, 241 (1958).
- [18] T. Moriya, Anisotropic superexchange interaction and weak ferromagnetism, *Phys. Rev.* **120**, 91 (1960).
- [19] I. E. Dzyaloshinskii, Theory of helicoidal structures in antiferromagnets. I. nonmetals, *Sov. Phys. JETP* **19**, 960 (1964).
- [20] Y. Togawa, T. Koyama, K. Takayanagi, S. Mori, Y. Kousaka, J. Akimitsu, S. Nishihara, K. Inoue, A. S. Ovchinnikov, and J. Kishine, Chiral Magnetic Soliton Lattice on a Chiral Helimagnet, *Phys. Rev. Lett.* **108**, 107202 (2012).
- [21] A. N. Bogdanov and D. A. Yablonskii, Thermodynamically stable “vortices” in magnetically ordered crystals. The mixed state of magnets, *Zh. Eksp. Teor. Fiz.* **95**, 178 (1989) [*JETP* **68**, 101 (1989)].

- [22] S. Mühlbauer, B. Binz, F. Jonietz, C. Pfleiderer, A. Rosch, A. Neubauer, R. Georgii, and P. Böni, Skyrmion lattice in a chiral magnet, *Science* **323**, 915 (2009).
- [23] X. Z. Yu, N. Kanazawa, Y. Onose, K. Kimoto, W. Z. Zhang, S. Ishiwata, Y. Matsui, and Y. Tokura, Near room-temperature formation of a skyrmion crystal in thin-films of the helimagnet FeGe, *Nat. Mater.* **10**, 106 (2011).
- [24] J. Kishine and A. S. Ovchinnikov, Theory of monoaxial chiral helimagnet, *Solid State Phys.* **66**, 1 (2015).
- [25] Y. Togawa, Y. Kousaka, K. Inoue, and J. Kishine, Symmetry, structure, and dynamics of monoaxial chiral magnets, *J. Phys. Soc. Jpn.* **85**, 112001 (2016).
- [26] Y. Togawa, T. Koyama, Y. Nishimori, Y. Matsumoto, S. McVitie, D. McGrouther, R. L. Stamps, Y. Kousaka, J. Akimitsu, S. Nishihara, K. Inoue, I. G. Bostrem, V. E. Sinitsyn, A. S. Ovchinnikov, and J. Kishine, Magnetic soliton confinement and discretization effects arising from macroscopic coherence in a chiral spin soliton lattice, *Phys. Rev. B* **92**, 220412 (2015).
- [27] A. Neubauer, C. Pfleiderer, B. Binz, A. Rosch, R. Ritz, P. G. Niklowitz, and P. Böni, Topological Hall Effect in the A Phase of MnSi, *Phys. Rev. Lett.* **102**, 186602 (2009).
- [28] J. Yonemura, Y. Shimamoto, T. Kida, D. Yoshizawa, Y. Kousaka, S. Nishihara, F. J. T. Goncalves, J. Akimitsu, K. Inoue, M. Hagiwara, and Y. Togawa, Magnetic solitons and magnetic phase diagram of the hexagonal chiral crystal CrNb₃S₆ in oblique magnetic fields, *Phys. Rev. B* **96**, 184423 (2017).
- [29] Y. Kousaka, Y. Nakao, J. Kishine, M. Akita, K. Inoue, and J. Akimitsu, Chiral helimagnetism in T_{1/3}NbS₂ (T = Cr and Mn), *Nucl. Instrum. Methods Phys. Res., Sect. A.* **600**, 250 (2009).
- [30] Y. Kousaka, T. Koyama, K. Ohishi, K. Kakurai, V. Hutano, H. Ohsumi, T. Arima, A. Tokuda, M. Suzuki, N. Kawamura, A. Nakao, T. Hanashima, J. Suzuki, J. Campo, Y. Miyamoto, A. Sera, K. Inoue, and J. Akimitsu, Monochiral helimagnetism in homochiral crystals of CsCuCl₃, *Phys. Rev. Mater.* **1**, 071402 (2017).
- [31] See Supplemental Material at <http://link.aps.org/supplemental/10.1103/PhysRevLett.122.057206> for further details of electrical resistance data, data analysis of R_{EMC}, and comparison of EMC coefficients among various materials, which includes Ref. [32].
- [32] N. Kanazawa, Y. Onose, T. Arima, D. Okuyama, S. Wakimoto, K. Kakurai, S. Ishiwata, and Y. Tokura, Large Topological Hall Effect in a Short-Period Helimagnet MnGe, *Phys. Rev. Lett.* **106**, 156603 (2011).
- [33] N. Nagaosa, J. Sinova, S. Onoda, A. H. MacDonald, and N. P. Ong, Anomalous Hall effect, *Rev. Mod. Phys.* **82**, 1539 (2010).
- [34] S. V. Grigoriev, S. V. Maleyev, A. I. Okorokov, Yu. O. Chetverikov, and H. Eckerlebe, Field-induced reorientation of the spin helix in MnSi near T_c, *Phys. Rev. B* **73**, 224440 (2006).
- [35] S. V. Grigoriev, S. V. Maleyev, E. V. Moskvina, V. A. Dyadkin, P. Fouquet, and H. Eckerlebe, Crossover behavior of critical helix fluctuations in MnSi, *Phys. Rev. B* **81**, 144413 (2010).
- [36] C. Pappas, L. J. Bannenberg, E. Lelièvre-Berna, F. Qian, C. D. Dewhurst, R. M. Dalgliesh, D. L. Schlagel, T. A. Lograsso, and P. Falus, Magnetic Fluctuations, Precursor Phenomena, and Phase Transition in MnSi under a Magnetic Field, *Phys. Rev. Lett.* **119**, 047203 (2017).
- [37] K. Tsuruta, M. Mito, H. Deguchi, J. Kishine, Y. Kousaka, J. Akimitsu, and K. Inoue, Nonlinear magnetic responses at the phase boundaries around helimagnetic and skyrmion lattice phases in MnSi: Evaluation of robustness of non-collinear spin texture, *Phys. Rev. B* **97**, 094411 (2018).
- [38] H. Wilhelm, M. Baenitz, M. Schmidt, U. K. Rößler, A. A. Leonov, and A. N. Bogdanov, Precursor Phenomena at the Magnetic Ordering of the Cubic Helimagnet FeGe, *Phys. Rev. Lett.* **107**, 127203 (2011).
- [39] A. Barla, H. Wilhelm, M. K. Forthaus, C. Strohm, R. Ruffer, M. Schmidt, K. Koepf, U. K. Rößler, and M. M. Abd-Elmeguid, Pressure-Induced Inhomogeneous Chiral-Spin Ground State in FeGe, *Phys. Rev. Lett.* **114**, 016803 (2015).
- [40] J. D. Bocarsly, R. F. Need, R. Seshadri, and S. D. Wilson, Magnetoentropic signatures of skyrmionic phase behavior in FeGe, *Phys. Rev. B* **97**, 100404 (2018).
- [41] I. Živković, J. S. White, H. M. Rønnow, K. Prša, and H. Berger, Critical scaling in the cubic helimagnet Cu₂OSeO₃, *Phys. Rev. B* **89**, 060401 (2014).
- [42] Y. Togawa, Y. Kousaka, S. Nishihara, K. Inoue, J. Akimitsu, A. S. Ovchinnikov, and J. Kishine, Interlayer Magneto-resistance Due to Chiral Soliton Lattice Formation in Hexagonal Chiral Magnet CrNb₃S₆, *Phys. Rev. Lett.* **111**, 197204 (2013).
- [43] N. J. Ghimire, M. A. McGuire, D. S. Parker, B. Sipoş, S. Tang, J.-Q. Yan, B. C. Sales, and D. Mandrus, Magnetic phase transition in single crystals of the chiral helimagnet Cr_{1/3}NbS₂, *Phys. Rev. B* **87**, 104403 (2013).
- [44] E. M. Clements, R. Das, L. Li, P. J. Lampen-Kelley, M.-H. Phan, V. Keppens, D. Mandrus, and H. Srikanth, Critical behavior and macroscopic phase diagram of the monoaxial chiral helimagnet Cr_{1/3}NbS₂, *Sci. Rep.* **7**, 6545 (2017).
- [45] T. Shishidou *et al.* (private communication).
- [46] R. Aoki, Y. Togawa, and S. Ohara, Electrical transport properties of micrometer-sized samples of the rare-earth chiral magnet YbNi₃Al₉, *Phys. Rev. B* **97**, 214414 (2018).